Comparative Study of Cohesive Zone and Virtual Crack Closure Techniques for Three-Dimensional Fatigue Debonding

A. PIRONDI[1], G. GIULIESE[1], F. MORONI[2], A. BERNASCONI[3], and A. JAMIL[3]

[1]*Dipartimento di Ingegneria Industriale, Università di Parma, Parma, Italy*
[2]*Centro Interdipartimentale SITEIA.PARMA, Università di Parma, Parma, Italy*
[3]*Dipartimento di Meccanica, Politecnico di Milano, Milano, Italy*

1. INTRODUCTION

Composite and hybrid metal/composite structures are nowadays present not only in the aerospace industry, but thanks to continuous performance improvement and cost reduction, also many more industrial fields are approaching the use of multimaterial structural elements. This requires, in turn, extensive use of adhesive bonding and a more and more sophisticated capability to simulate and predict the strength of bonded connections where, for this purpose, analytical methods are being progressively integrated or

Received 17 July 2013; in final form 23 October 2013.

Address correspondence to A. Pirondi, Dipartimento di Ingegneria Industriale, Università di Parma, Parco Area delle Scienze 181/A, 43124 Parma, Italy

replaced by finite element analysis (FEA). In engineering applications, it is well established that fatigue is the root cause of many structural failures. In the case of bonded joints, fatigue life is related to the initiation and propagation of defects starting at free edges of joining regions or other features, such as through-thickness holes. In the case of composite or metal/composite joints, fatigue can start also from defects at the same locations cited above, with the difference that the crack may either run into the adhesive or become a delamination crack. Especially in the case of damage tolerant or fail safe design, it is necessary to know how cracks, or in general defects, propagate during the service life of a component. A numerical method able to reproduce three-dimensional fatigue debonding in structures is therefore necessary to improve their performances.

The relationship between the applied stress intensity factor and the fatigue crack growth (FCG) rate of a defect is generally expressed as a power law [1]. In the case of polymers, adhesives, and composites, the relationship is traditionally written as a function of the range of strain energy release rate (ΔG) as

$$\frac{da}{dN} = B\Delta G^d, \tag{1}$$

where B and d are parameters depending on the material and load mixity ratio, and a is the defect length. In this simple form, the presence of a fatigue crack growth threshold and an upper limit to ΔG for fracture are not represented although, when needed, expressions accounting for these limits can be easily found (see for example [2]). In the same way, the influence of the stress ratio, R, on the fatigue crack growth rate can be introduced into Eq. (1) by a term derived from extensions of the Paris law expressed in terms of the range of stress intensity factor, ΔK [3].

When a solution for the strain energy release rate as a function of crack length exists, then the number of cycles to failure comes out from the numerical integration between the initial crack length (a_0) and the final crack length (a_f) of the inverse of Eq. (1) ([2,4]).

When a theoretical solution for the strain energy release rate does not exist, finite element (FE) simulation is commonly used to compute it. The prediction of crack growth can be then carried out by a stepwise analysis, each step corresponding to a user-defined crack growth increment and the number of cycles is obtained by integrating the crack growth rate computed from the Paris law. To speed up the process, in some finite element software, this procedure is integrated in special features (for example the *Debonding procedure in Abaqus®, Dassault Systèmes, Paris, France), where the strain energy release rate is obtained using the Virtual Crack Closure Technique (VCCT).

An alternative way for dealing with fatigue crack growth problems is using the cohesive zone model (CZM). This model is commonly used for the simulation of the quasi-static fracture problems, especially in the case

of interface cracks such as in bonded joints and delamination in composites ([5–7], among others). The possibility to simulate the growth of a crack without any remeshing requirements and the relatively easy possibility to manipulate the constitutive law of the cohesive elements makes the cohesive zone model attractive also for the fatigue crack growth simulation [8–19]. However, differently from VCCT, three-dimensional fatigue debonding/delamination with CZM is not yet state of art in finite element software. The aim of this paper is therefore to compare the CZM, developed in reference [20] for three-dimensional simulation of fatigue crack growth in mode I loaded assemblies and extended to mixed-mode I/II loaded assemblies in [21], with the VCCT model embedded in the software Abaqus (v. 6.11) in order to assess the correspondence of the results in terms of crack growth prediction and computation time. The comparison has been done on mode I, mode II, and mixed-mode I/II loaded cracks in bonded assemblies.

2. CZM AND VCCT MODELS FORMULATION

2.1. VCCT

Based on linear elastic fracture mechanics (LEFM), VCCT is a well-known technique for the evaluation of strain energy release rate (SERR) and mode–mixity ratio for cracks in homogeneous materials [22–48]. It is based on the equality between the strain energy released, when a crack is extended by a certain amount δa and the work done by crack tip nodal forces to virtually close it of the same amount δa. Additionally, crack growth self-similarity is invoked. With the help of this assumption, the same model is used for the extraction of reaction forces and displacements required to close the crack by Δa and thus the two step crack closure method reduces to one step virtual crack closure method (Fig. 1).

In order to calculate the SERR using two-dimensional finite element models in either plane stress or plane strain conditions, an advancing crack is considered with an initial crack front at a point l, the point l splits into two points l_1 and l_2 forming a new crack front at point i as seen in Fig. 2. If u and u' are the displacements in local x-direction and v and v' are the displacements in the y-direction of the points l_1 and l_2, respectively, then the strain energy release rate G, based on VCCT can be evaluated as follows:

$$G_{\mathrm{I}} = \frac{1}{2t\delta a} F_y(v - v'),$$
$$G_{\mathrm{II}} = \frac{1}{2t\delta a} F_x(u - u'), \tag{2}$$

The total energy release rate is $G = G_{\mathrm{I}} + G_{\mathrm{II}}$ and

T Out-of-plane width
Δa Element length

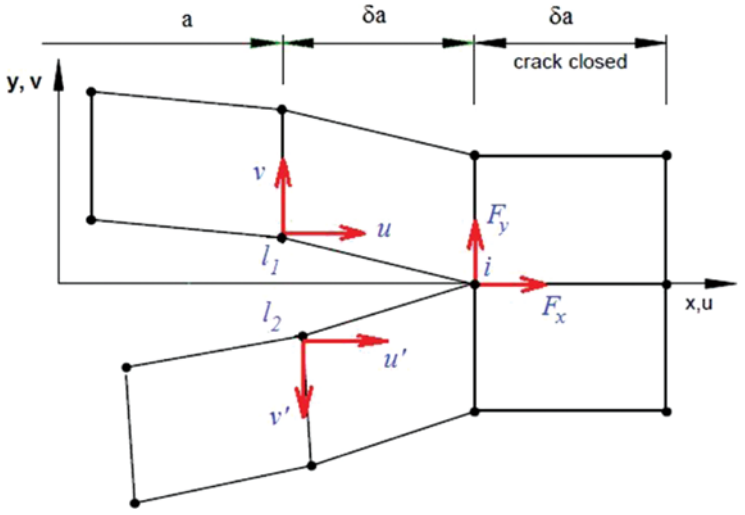

FIGURE 1 Modified crack closure method with single step (one step VCCT).

F_x Force per unit length on node i in x-direction
F_y Force per unit length on node i in y-direction
Δu Difference of displacements between nodes l_1 and l_2
Δv Difference of displacements between nodes l_1 and l_2

VCCT is implemented in Abaqus® for both two and three dimensions. In a two-dimensional problem, the crack is represented as a one-dimensional discontinuity formed by a line of nodes with the bulk material located on both sides of the discontinuity. The bulk material is modeled in the form of two distinct parts joined together by means of a contact pair all along the discontinuity, having either of the coinciding edges to be a master surface

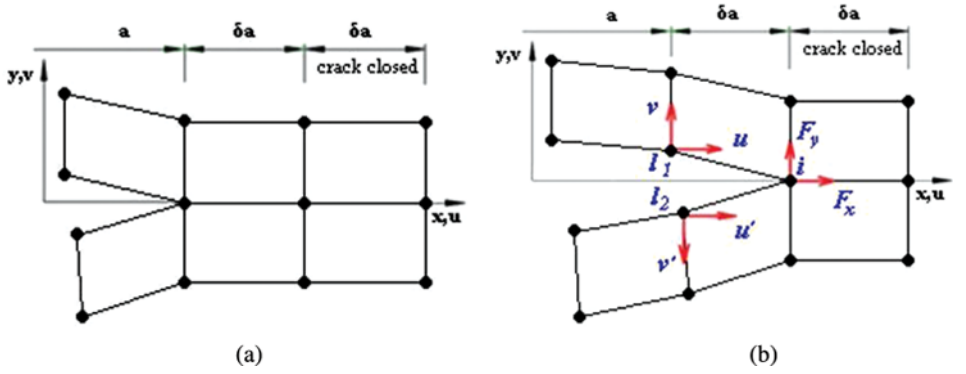

FIGURE 2 Crack extension of the crack from point *l* to point *i*: (a) before and (b) after extension.

and the other to be a slave surface. The nodes on the discontinuity share the same coordinates and play an important role in the definition of pre-cracked region, the crack front, and the crack path.

The nodes on the discontinuity, which are not bonded and free to move away from each other, represent the pre-crack region, whereas the nodes which are bonded and stuck to each other, referred to as bonded nodes, define the crack propagation path. The point of transition of bonded and unbonded nodes forms the crack front. It is possible to define a completely bonded interface; however, at least one node has to be kept initially unbonded for the identification of the crack front. Normal surface behavior is specified for the contact pair as with no penetration and bonding is set as initial condition for the bonded portion of contact pair, while debonding during analysis is set by a specific card (*DEBOND). The debonding of nodes follows Eq. (1) by setting the appropriate criterion (*DEBOND, TYPE = FATIGUE), where the coefficients B and d are however taken independent of the mixed-mode ratio.

2.1.1. Direct cyclic analysis

Fatigue crack growth is done in Abaqus® within the Direct Cyclic procedure, which is a quasi-static analysis using a combination of Fourier series and iterative time integration of nonlinear material behavior by with the modified Newton method. The elastic stiffness matrix at the beginning of the analysis step serves as Jacobian for obtaining the stabilized response of an elastic–plastic structure subjected to constant amplitude cyclic loading. It effectively provides the cyclic response of the structure directly by neglecting the pre-stability loading cycles of a transient analysis, which are numerically quite expensive. The method is based on the development of a displacement function $F(t)$ which describes the structural response at all moments of time t, in a loading cycle, within a given time period T. This function is represented in the following way:

$$U(t) = U_o + \sum_{k=1}^{n} \left[U_k^s \sin k\omega t + U_k^c \cos k\omega t \right], \tag{3}$$

where n represents the number of terms in the Fourier series, ω is the angular frequency, and U_0, U_k^s, and U_k^c are the coefficients of displacement corresponding to each degree of freedom. The residual vectors are of the same form as the displacement function and are represented by

$$R(t) = R_o + \sum_{k=1}^{n} \left[R_k^s \sin k\omega t + R_k^c \cos k\omega t \right], \tag{4}$$

where R_o, R_k^s, and R_k^c have the same correspondence with the displacement coefficients U_0, U_k^s, and U_k^c, respectively, and this vector $R(t)$ is tracked for each instance of time in the loading cycle by using element to element calculations. The integration of this function $R(t)$ over the entire cycle yield the following Fourier coefficients

$$R_0 = \frac{2}{T}\int_0^T R(t)\mathrm{d}t,$$

$$R_k^s = \frac{2}{T}\int_0^T R(t)\sin k\omega t\mathrm{d}t, \tag{5}$$

$$R_k^s = \frac{2}{T}\int_0^T R(t)\cos k\omega t\mathrm{d}t.$$

These coefficients correspond to the displacement coefficients and are then compared with the tolerance defined in the step to achieve convergence. If the tolerance is met, convergence is achieved and the solution is obtained for that loading cycle. However, when these residuals are larger than the tolerance parameters then correction parameter c_k is evaluated in which corrections to the displacement coefficients c_0, c_k^s, and c_k^c are made in the following way:

$$U_0^{(i+1)} = U_0^{(i)} + c_0^{(i+1)},$$

$$U_k^{c(i+1)} = U_k^{c(i)} + c_k^{c(i+1)}, \tag{6}$$

$$U_k^{s(i+1)} = U_k^{s(i)} + c_k^{s(i+1)}.$$

The updated displacement coefficients are used in the next iteration to obtain displacements at each instant in time. This process is repeated until convergence is obtained. Each pass through the complete load cycle can therefore be thought of as a single iteration of the solution to the nonlinear problem.

2.2. Cohesive Zone Model

Although different and complicated shapes of the cohesive law are proposed in the literature, the triangular one (Fig. 3) is taken as it is often good enough to describe crack growth behavior. In that case, damage starts once the tripping stress $\sigma_{ij\max}$ (i, j = 1, 2) has been attained, decreasing progressively the element stiffness K_{ij}. However, the model "as is" does not incorporate subcritical damage

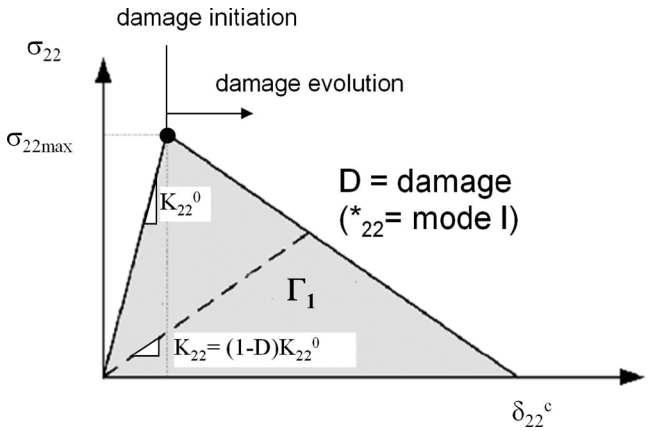

FIGURE 3 Example of a triangular cohesive law.

accumulation, *i.e.*, cyclic damage is not possible below δ_{ij}^{0} and does not accumulate beyond the first cycle above. The model for 3D cyclic cohesive damage formulated by some of the authors in reference [21] is reported in the following. In this model, the concept proposed in reference [12] is retained, while fundamental differences with respect to that work concern: (i) the damage D is related directly to its effect on stiffness and not to the ratio between the energy dissipated during the damage process and the cohesive energy and then, in turn, to the stiffness; (ii) the process zone size A_{CZ} is defined as the sum of A_e of the cohesive elements for which the difference in opening between the maximum and minimum load of the fatigue cycle, $\Delta\delta = \delta_{max} - \delta_{min}$, is higher than a threshold value $\Delta\delta$th; therefore, it is evaluated by FEA during the simulation and not derived from a theoretical model; (iii) the strain energy release rate is calculated using the contour integral method over the cohesive process zone and it is implemented as a user-defined field subroutine (USDFLD) in Abaqus acting on standard cohesive elements, instead of a user element.

Considering a representative surface element (represented in the simulation by a cohesive element section pertaining to one integration point, Fig. 4) with a nominal surface equal to A_e, the accumulated damage can be related to the damaged area due to micro voids or crack (A_d):

$$D = \frac{A_d}{A_e}. \tag{7}$$

In reference [12], D is related to the ratio between the energy dissipated during the damage process and the cohesive energy (Γ_{22} in Fig. 3) and then, in turn, to the stiffness. In the present model instead, D acts directly on stiffness, alike in [49]. Referring to a mode I loading case, when the opening is relatively small the cohesive element behaves linearly; this happens until a given value of displacement, $\delta_{22,0}$ (or equivalently until a certain value of

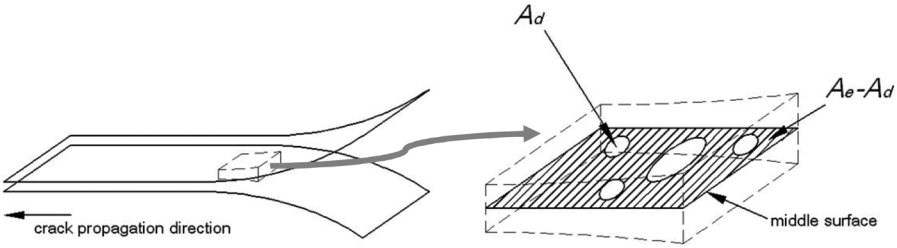

FIGURE 4 Nominal and damaged area in a representative surface element (RSE).

stress $\sigma_{22,0}$). This initial step is characterized by a stiffness $K_{22,0}$, that remains constant until $\delta_{22,0}$. Beyond this limit the stiffness is progressively reduced by D, until the final fracture in $\delta_{22,C}$ where the two surfaces are completely separated. Between $\delta_{22,0}$ and $\delta_{22,C}$ the stiffness K_{22} can be computed as

$$K_{22} = K_{22,0}(1 - D). \tag{8}$$

The area Γ_{22} underling the cohesive law is the energy to make the defect grow of a unit area and it is therefore representative of the fracture toughness, G_{IC},

$$\Gamma_{22} = \int_0^{\delta_C} \sigma_{22} d\delta_{22}. \tag{9}$$

In the monotonic case, the damage variable D can be written as a function of the opening (δ_{22}) and of the damage initiation and critical opening (respectively $\delta_{22,0}$ and $\delta_{22,C}$):

$$D = \frac{\delta_{22,c}\left(\delta_{22} - \delta_{22,0}\right)}{\delta_{22}\left(\delta_{22,c} - \delta_{22,0}\right)}. \tag{10}$$

When the element is unloaded, the damage cannot be healed; therefore, looking at Fig. 3, the unloading and subsequent loadings will follow the dashed line, until a further damage is attained. This simple model is able to describe the monotonic damage in case of mode I loading.

Considering the entire cohesive layer, the areal crack extension (A) can be computed as the sum of damaged areas of all the cohesive elements integration points (A_d) [12]:

$$A = \sum A_\mathrm{d}. \tag{11}$$

When the fatigue damage is considered, from the previous equation, the crack growth (dA) can be written as a function of the increment of the damage area of all the cohesive elements (dA_d), therefore:

$$dA = \sum dA_\mathrm{d} \tag{12}$$

However the damage increment would not concern the whole cohesive layer, but it will be concentrated in a relatively small process zone close to the crack tip. In order to estimate the size of A_{CZ}, analytical relationships can be found in the literature [50], where the size per unit thickness is defined as the distance from the crack tip to the point where $\sigma_{22,0}$ is attained. In this work, a different definition and evaluation method is proposed: A_{CZ} corresponds to the sum of the nominal sections of the cohesive elements where the difference in opening between the maximum and minimum load of the fatigue cycle, $\Delta\delta_{22} = \delta_{22,\max} - \delta_{22,\min}$, is higher than a threshold value $\Delta\delta_{22}$th. The value $\Delta\delta_{22}$th is supposed to be the highest value of $\Delta\delta_{22}$ in the cohesive layer when ΔG in the simulation equals ΔG_{th} experimentally obtained by FCG tests. It has to be underlined that in this way FCG may take place even at $\delta_{22,\max} \leq \delta_{22,0}$, which is a condition that should be accounted for since $\delta_{22,0}$ results from the calibration of cohesive zone on fracture tests and may not be representative of a threshold for FCG. The process zone size A_{CZ} has therefore to be evaluated by FEA while performing the FCG simulation but, on the other hand, does not need to be assumed from a theoretical model.

Equation (12) can be therefore rewritten as follows [12]:

$$\mathrm{d}A = \sum_{i \in A_{CZ}} \mathrm{d}A_{\mathrm{d}}^{i}, \tag{13}$$

where only the elements lying in the process zone (named A_{CZ}) are considered.

In order to represent the crack growth due to fatigue ($\mathrm{d}A/\mathrm{d}N$), the local damage of the cohesive elements (D) has to be related to the number of cycles (N). This is done using the following equation:

$$\frac{\mathrm{d}D}{\mathrm{d}N} = \frac{\mathrm{d}D}{\mathrm{d}A_{\mathrm{d}}} \frac{\mathrm{d}A_{\mathrm{d}}}{\mathrm{d}N} \tag{14}$$

The first part of Eq. (14) can be easily obtained deriving Eq. (7); therefore,

$$\frac{\mathrm{d}D}{\mathrm{d}A_{\mathrm{d}}} = \frac{1}{A_{\mathrm{e}}}. \tag{15}$$

The process to obtain the second part is quite more complicated: the derivative of Eq. (13) with respect to the number of cycles is

$$\frac{\mathrm{d}A}{\mathrm{d}N} = \sum_{i \in A_{CZ}} \frac{\mathrm{d}A_{\mathrm{d}}^{i}}{\mathrm{d}N}. \tag{16}$$

At this point, an assumption is introduced: the increment of damage per cycle is supposed to be the same for all the elements lying in the process zone.

Therefore, the value dA_d/dN is assumed to be the average value of the damaged area growth rate dA_d^i/dN for all of the elements in the process zone.

Hence the crack growth rate can be rewritten as [12]:

$$\frac{dA}{dN} = \sum_{i \in A_{CZ}} \frac{dA_d}{dN} = n_{CZ} \frac{dA_d}{dN} \tag{17}$$

where n_{cz} is the number of elements lying on the process area A_{CZ}. n_{cz} can be written as the ratio between the process zone extension (A_{CZ}) and the nominal cross-sectional area (A_e) leading to the equation:

$$\frac{dA}{dN} = \frac{A_{CZ}}{A_e} \frac{dA_d}{dN}. \tag{18}$$

The second part of Eq. (14) can be therefore written as follows:

$$\frac{dA_d}{dN} = \frac{dA}{dN} \frac{A_e}{A_{CZ}}. \tag{19}$$

Combining Eqs. (15) and (19), the crack growth rate can be finally expressed as a function of the applied strain energy release rate, in the simplest version using Eq. (1):

$$\frac{dD}{dN} = \frac{1}{A_{CZ}} B \Delta G^d. \tag{20}$$

2.2.1. Strain energy release rate computation

The relationship between the applied strain energy release rate and the increase of damage in the cohesive zone needs a general method to calculate the value of the strain energy release rate as a function of crack length. The most common methods for the strain energy release rate evaluation by using the FEA are the contour integral (J) and the VCCT. These two methods are usually available in finite element software, but VCCT is intended in general as alternative to using cohesive elements while the software used in this work (Abaqus®) does not output the contour integral for an integration path including cohesive element.

In order to compute the J-integral, a path surrounding the crack has to be selected. Considering, for example, the crack in Fig. 5, the path (Ω) is displayed by the dashed line and it is represented by the top and bottom nodes of the cohesive elements.

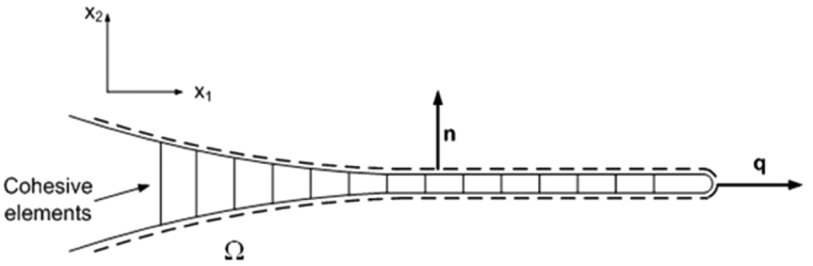

FIGURE 5 Example of *J*-integral surrounding the cohesive element layer.

The *J*-integral definition [51] is

$$J = \int_{\Omega} \mathrm{n} \cdot [H] \cdot \mathrm{q} \mathrm{d}\Omega \tag{21}$$

where n is a vector normal to the path, q is a vector lying on the crack propagation direction, and $[H]$ is defined as

$$[H] = W[I] - \left[\sigma_{ij}\right]\left[\frac{\partial u_{ij}}{\partial x_{ij}}\right], \tag{22}$$

where W is the strain energy density, $[\sigma_{ij}]$ the stress matrix, and u_i the displacements of the points lying on the path.

Neglecting geometrical nonlinearity, the vector q can be assumed to be perpendicular to the direction x_2 along the whole path; therefore, the *J*-integral can be rewritten as follows:

$$J = \int_{\Omega} \left(-\sigma_{12}\frac{\partial u_1}{\partial x_1} - \sigma_{22}\frac{\partial u_2}{\partial x_1}\right)\mathrm{d}\Gamma. \tag{23}$$

Extracting the opening/sliding and the stresses in the cohesive elements at the beginning of the increment, the strain energy release rate is then computed. An interesting feature of this approach is that the mode I and the mode II component of the *J*-integral can be obtained by integrating separately the second or the first components of the integral in Eq. (23), respectively.

This method can be easily implemented for a two-dimensional problem, since there is only one possible path. In the case of three dimensional problems, the implementation is more difficult since several paths can be identified along the crack width, and moreover their definition is rather troublesome, especially when dealing with irregular meshes. A three-dimensional version has been implemented in [21] in the case of planar crack geometries and regular cohesive mesh. In this case, Eq. (23) is evaluated on several parallel contours in order to obtain *J*-integral along the crack front.

2.2.2. Finite element implementation

The theoretical framework described in Section 2.2 and the strain energy release rate (SERR) calculation procedures are implemented programming Fortran subroutines templates available in the commercial software Abaqus®. In particular the USDFLD Abaqus® subroutine is used to modify the cohesive element stiffness by means of a field variable that accounts for damage, while the URDFIL subroutine is used to get the results in terms of stresses, displacements, and energies. The fatigue analysis is carried out a as a simple static analysis divided in a certain number of increments. Each increment corresponds to a given number of cycles.

Assuming that the fatigue cycle load varies from a maximum value $P_{\max}$ to a minimum value $P_{\min}$, the analysis is carried out applying to the model the maximum load $P_{\max}$. The load ratio is defined as the ratio between the minimum and maximum load applied:

$$R = \frac{P_{\max}}{P_{\min}}. \tag{24}$$

The strain energy release rate amplitude is, therefore,

$$\Delta G = \left(1 - R^2\right) G_{\max}. \tag{25}$$

This latter is compared with the strain energy release rate threshold ΔG_{th}. If $\Delta G > \Delta G_{\text{th}}$, the analysis starts (or it continues is the increment is not the first) otherwise the analysis is stopped.

The flow diagram in Fig. 6 shows the operations done within each increment, where ΔD_i^j is calculated as follows:

$$\begin{aligned} \Delta D_i^j &= \Delta D_{\max} \qquad \text{if } 1 - D_i^j > \Delta D_{\max}, \\ \Delta D_i^j &= 1 - D_i^n \qquad \text{if } 1 - D_i^j < \Delta D_{\max}. \end{aligned} \tag{26}$$

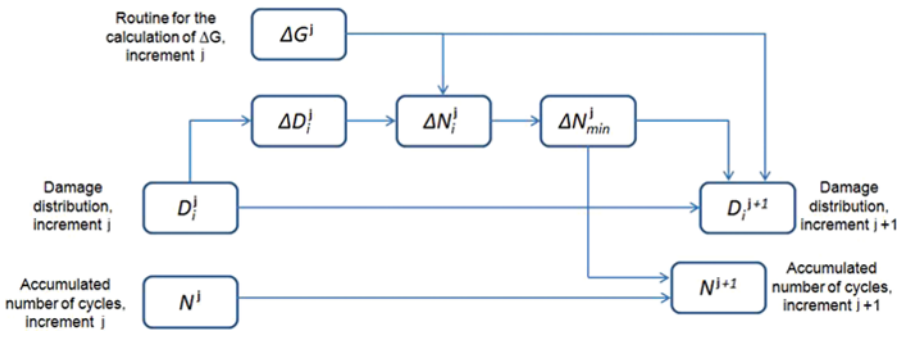

FIGURE 6 Flow diagram of the automatic procedure for the crack growth rate prediction.

In other words, ΔD_i^j is the minimum between the $\Delta D_{\max}$ and the amount needed for D to reach the unity. The procedure is explained in detail in reference [19].

It is worth to underline that the procedure is fully automated, *i.e.*, the simulation is performed in a unique run without stops. During the initial loading ramp, the stress–strain behavior is represented by the input cohesive law and the statically accumulated damage, represented by Eq. (10), is stored for the cohesive elements where $\delta > \delta_0$. The stiffness is then degraded according to the procedure described previously, starting from the stored static value until $D = 1$. If $\delta_{\max}$ of the cycle is lower than δ_0 but $\Delta\delta > \Delta\delta_{\text{th}}$, elements entering the process zone during the fatigue analysis step start damaging before $\delta > \delta_0$. In this case, the stress deviates from the linear elastic region of the cohesive law at $d<\bar{o}_0$ to fall then on the linear damage part without reaching $\sigma_{\max}$.

Whenever a static overload occurs at a certain point in life, the cohesive element responds elastically with a degraded stiffness K instead of K_0, and further damage, or even static crack growth, can be accumulated related to the overload according to Eq. (10). After the overload, cyclic loading starts from the value of cyclic +static damage stored previously, see reference [52].

2.2.3. MIXED-MODE LOADING

With the aim to extend the model to mixed-mode I/II conditions, a mixed-mode cohesive law has to be defined. This is done according to the scheme shown in Fig. 7 from the knowledge of the pure mode I and pure mode II cohesive laws (the index 22, refers to opening or mode I direction, index 12 refers to sliding or mode II direction)

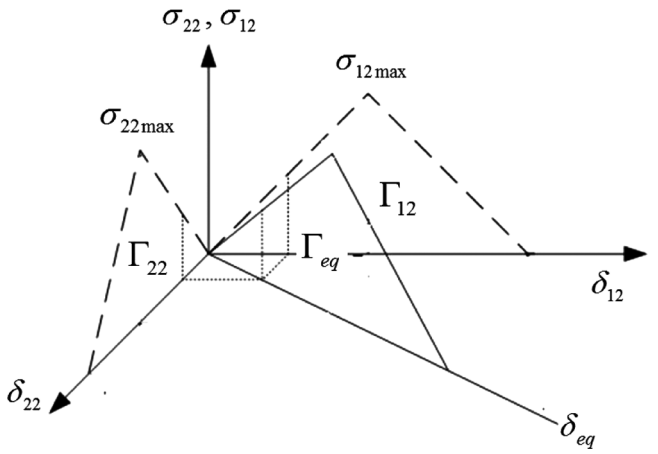

FIGURE 7 Example of cohesive law in the case of mixed-mode conditions.

First of all the mixed-mode equivalent opening has to be defined. This is done using the relationship:

$$\delta_{\mathrm{eq}} = \sqrt{\left(\frac{\delta_{22} + |\delta_{22}|}{2}\right)^2 + (\delta_{12})^2}. \tag{27}$$

In case of pure mode I, this equation yields the value of δ_{22} in case of positive δ_{22}, while it gives 0 in case of negative δ_{22}. This is done since it is supposed that compression stresses do not lead to the damage of the adhesive layer. Of course δ_{22} assumes only positive values if crack surface interpenetration is properly prevented in the model. In the present model, interpenetration is prevented by restoring element stiffness if values of $\delta_{22} < 0$ are detected.

Moreover, the mixed-mode cohesive law is defined in terms of the initial stiffness ($K_{\mathrm{eq},0}$), damage initiation equivalent opening ($\delta_{\mathrm{eq},0}$), and critical equivalent opening ($\delta_{\mathrm{eq,C}}$). The equivalent initial stiffness is obtained by equating the equivalent strain energy (U_{EQ}) to the total strain energy (U_{TOT}), which in turn is equal to the sum of the strain energy in mode I (U_{22}) and in mode II (U_{12}):

$$U_{\mathrm{EQ}} = U_{\mathrm{TOT}} = U_{22} + U_{12} = \frac{1}{2} \cdot \delta_{\mathrm{eq}}^2 \cdot K_{\mathrm{eq}}^0 = \frac{1}{2} \cdot (\delta_{22} + |\delta_{22}|)^2 \cdot K_{22}^0 + \frac{1}{2} \cdot \delta_{12}^2 \cdot K_{12}^0, \tag{28}$$

where $K_{22,0}$ and $K_{12,0}$ represent the initial stiffness of the mode I and mode II cohesive laws, respectively.

A further relationship is needed to define damage initiation: this is done using the quadratic damage initiation criterion [53]:

$$\left(\frac{\sigma_{22}}{\sigma_{22\,\max}}\right)^2 + \left(\frac{\sigma_{12}}{\sigma_{12\,\max}}\right)^2 = 1. \tag{29}$$

The last relationship needed, regards the definition of the critical equivalent opening. Since the area underlying the cohesive law is representative of the critical strain energy release rate, using the Kenane and Benzeggagh (KB) theory [54] the area underlying the mixed-mode equivalent cohesive law (Γ_{eq}) can be computed as

$$\Gamma_{\mathrm{eq}} = \Gamma_{22} + (\Gamma_{12} - \Gamma_{22}) \cdot MM^{\mathrm{m_m}}, \tag{30}$$

where (Γ_{22}) and (Γ_{12}) are the areas underlying the mode I and mode II cohesive laws, respectively; $\mathrm{m_m}$ is a mixed-mode coefficient depending on the adhesive; and MM is the mixed-mode ratio defined as a function of the mode I and mode II strain energy release rates as follows:

$$MM = \frac{G_{\mathrm{II}}}{G_{\mathrm{I}} + G_{\mathrm{II}}}. \tag{31}$$

The KB mixed-mode fatigue crack propagation model [55] is the first considered, since it is the most general law that can be found in the literature. The fatigue crack growth rate is given by Eq. (1), where this time B and d are functions of the mixed-mode ratio MM:

$$\ln B = \ln B_{\mathrm{II}} + (\ln B_{\mathrm{I}} - \ln B_{\mathrm{II}})(1 - MM)^{n_B}, \tag{32}$$

$$d = d_{\mathrm{I}} + (d_{\mathrm{II}} - d_{\mathrm{I}})(MM)^{n_d}, \tag{33}$$

and d_{I}, B_{I} and d_{II}, B_{II} are, respectively, the parameters of the Paris law in mode I and mode II and n_d, n_B are material parameters. Also other literature approaches were implemented in [19] but they are not considered here for the sake of comparison with Abaqus® VCCT fatigue delamination, where KB is the only mixed-mode loading FCG model. Moreover, updating of B and d with MM during propagation has been deactivated since it is not a feature available in Abaqus®.

2.3. Finite Element Models

The CZM and VCCT fatigue delamination models were tested on various joint geometries characterized by different mixed-mode ratios, in order to verify accuracy, robustness, and performance in terms of computational time. In particular, pure mode I loading was simulated with a Double Cantilever Beam (DCB) geometry, pure mode II loading with an End Loaded Split (ELS) geometry, and mixed-mode I/II loading with a Mixed-Mode End Loaded Split (MMELS) geometry, as shown in Fig. 8. Additionally, a single-lap joint (SLJ) was modeled as a representative case of real joint geometry (see

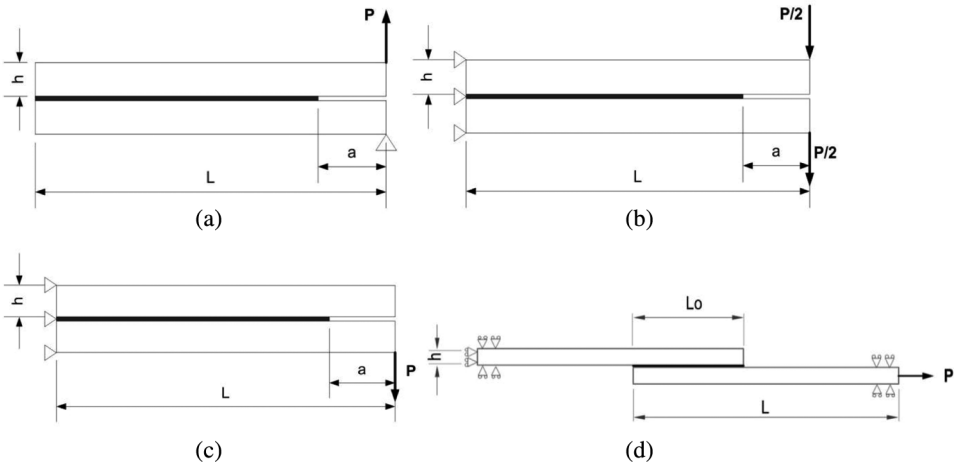

FIGURE 8 Simulated geometries: (a) DCB, (b) ELS, (c) MMELS, and (d) SLJ.

TABLE 1 Specimen Dimensions and the Applied Load for Unit Thickness

Parameter	Mode I	Mode II
Γ [N/mm]	0.266	1.002
σ_{max} [MPa]	30	30
δ_0 [mm]	0.003	0.003
δ_C [mm]	0.0173	0.066
B [$N^{-d}mm^{2-d}$]	0.0616	4.23
D	5.4	4.5

Parameter	Value
m_m	2.6
m_d	1.85
m_B	0.35

Fig. 8). Even though cracks may initiate from both sides of the SLJ, here the propagation was allowed only on one side to simplify the comparison of the two FCG models. The applied load and the specimens dimensions are given in Table 1. The elastic properties are taken as those typical of an aluminum alloy ($E = 70$ GPa; $\nu = 0.3$) while the cohesive law and FCG behavior is taken from [12]. All the properties are summarized in Table 2. In all the simulations a load ratio $R = 0$ is assumed. The adherends were meshed with 3D Continuum Shell elements and, in the case of CZM, the cohesive elements were kinematically tied to the two delaminating halves. The element size at the delamination plane was 0.5 mm (CZM) and 1.0 mm (VCCT) in order to keep computation time within a reasonable value. Other parameters to be set, specific of each FCG model, are as follows:

- a maximum damage increment, $\Delta D_{max} = 0.2$, based on the sensitivity analysis done in [56], has been used for CZM;
- a number of Fourier series terms equal to 49 and a time increment 0.01.

The choice of time increment in the VCCT solution followed from a convergence study. Indeed, a strong influence of time integration points was observed on the results obtained by VCCT and different values of SERR

TABLE 2 Cohesive Zone Parameters and FCG Behavior for Pure Mode I and Pure Mode II, and Mixed-Mode I/II [12]

	DCB	ELS	MMELS	SLJ
P [N/mm]	10	20	15	200
a_0 [mm]	20	20	20	/
b [mm]	5	5	5	10.56
L [mm]	175	175	175	285.8
b [mm]	20	20	20	20
Lo [mm]	/	/	/	110.8

were obtained when the time integration points were varied from 10 to 1000. As a result of these variations in SERR, there were significant differences in the estimation of the number of cycles due to the presence of high values of the exponent in the Paris Law. Therefore, 1000 time integration points with an initial time increment of 0.001 were used to evaluate accurate results which however, increased the computational time drastically.

An initial crack length equal to the size of one element has been specified for the SLJ when simulated using VCCT, while no initial crack length was needed in the case of CZM.

The increment in crack length was fixed in the case of VCCT, *i.e.*, equal to element size along the delaminating/debonding interface, while in the case of CZM it came as a result of in the increment in damage ΔD; therefore, it is not generally constant as ΔD may vary from increment to increment according to Eq. (26). However, the average increment in crack length in the case of CZM ranged from 0.1 to 0.5 mm in the various cases simulated in this work.

3. COMPARISON OF CZM AND VCCT PERFORMANCE

The two methods are compared with respect to: (i) agreement with each other; (ii) calculation time. Concerning (i), a comparison of G values along the crack front was done at selected crack lengths while, due to crack front bowing (Fig. 9), the average G (or G_{I}, G_{II}), and crack length along the crack front were considered for a global comparison. Additionally, Eq. (1) is integrated numerically using the G vs. crack length coming from the analysis instead of taking directly the output number of cycles. The reason is that, as the CZM process zone needs some time to get to a steady state while VCCT does not, the G calculated by CZM may be rather different in the first

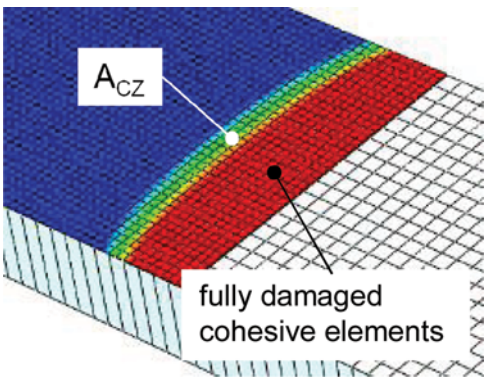

FIGURE 9 Bowed crack front and process zone in mode I fatigue modeling with CZM.

millimeters of propagation yielding a different number of cycles. For this reason, a comparison with experiments is foreseen as a further validation step, while at the moment the paper focuses on the comparison of numerical results of the two model after the transient phase of process zone formation. Regarding ii), the time the analyst has to wait for the crack to reach the knee of the *a*–*N* diagram, that is close to fracture, was monitored. In the cases examined, this means a crack length of 30 mm for all the geometries except SLJ, for which the analyses were stopped at 10 mm of crack length even though still far from fracture. Only the outputs strictly necessary for each model were required, in order to minimize time spent in storing data. The PC used for calculations for CZM was an Intel® Core™ I, −2630QM 2 GHz CPU, with 6 GB RAM and 579 Gb HD (7200 rpm, 6 MB cache), while for VCCT it was an Intel® Xeon™ E5645 (Nehalem, 1 core) 2.4 GHz CPU, with 48 GB RAM and 900 Gb HD (10 k rpm, 12.3 MB cache).

3.1. Strain Energy Release Rate Comparison

3.1.1. Mode I loading (DCB)

The two models show the same trend and an overall good correspondence with each other in Fig. 10, with CZM yielding generally slightly higher values than VCCT and a different trend in the first millimeter, where the process zone is under development. The average difference is about 5% on the 21–29-mm crack length span.

The main result in terms of crack length vs. number of cycles is shown in Fig. 11, where a 28% difference in number of cycles at 29 mm is evident, though compatible with the difference in G in Fig. 10. It is believed that further mesh refinement can get the two models closer to each other in this case.

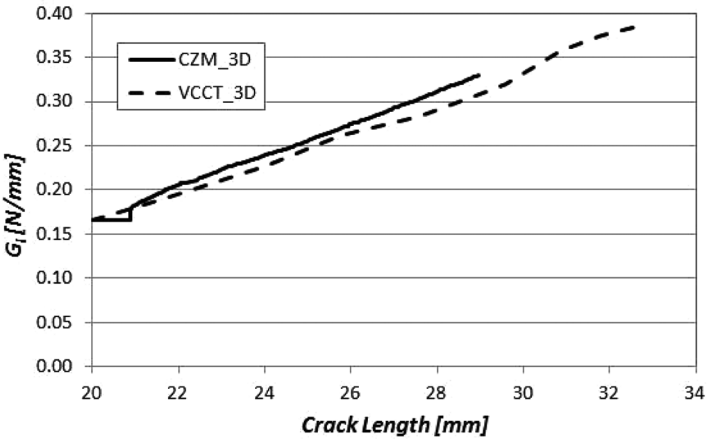

FIGURE 10 Comparison of G_I obtained by CZM and VCCT in the case of DCB.

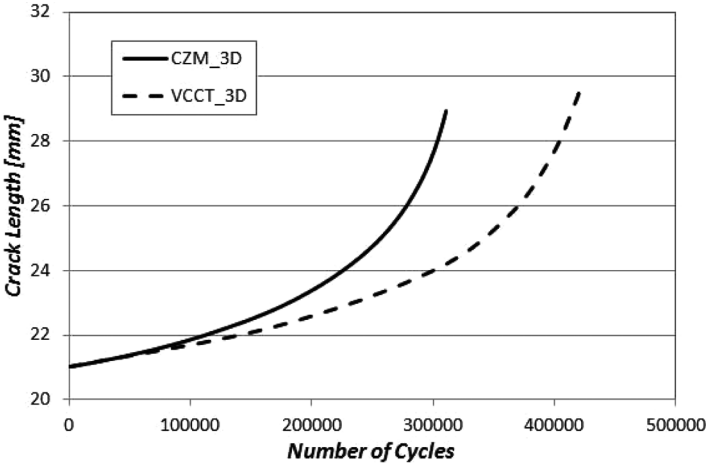

FIGURE 11 Comparison of *a*–*N* values in the case of DCB obtained by CZM and VCCT.

3.1.2. Mode II loading (ELS)

Figure 12 shows the values of G_{II} obtained by CZM and VCCT. Again as in the case of DCB, the two sets show a good overall correspondence with each other except the first millimeter and some oscillations in VCCT values probably related to a non-uniform (one row of elements per time increment) crack front propagation that has been recorded in the simulation.

The main result in terms of crack length vs. number of cycles is shown instead in Fig. 13, where a difference comes out lower than mode I (18% at 39-mm crack length), and also in this case a further mesh refinement can get the two models closer to each other.

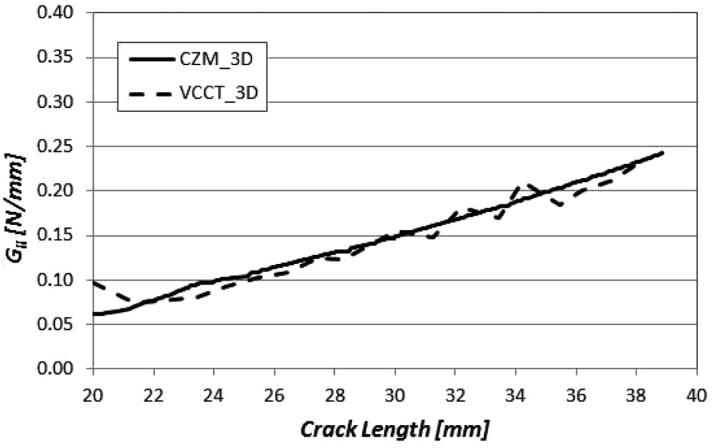

FIGURE 12 Comparison of G_{II} obtained by CZM and VCCT in the case of ELS.

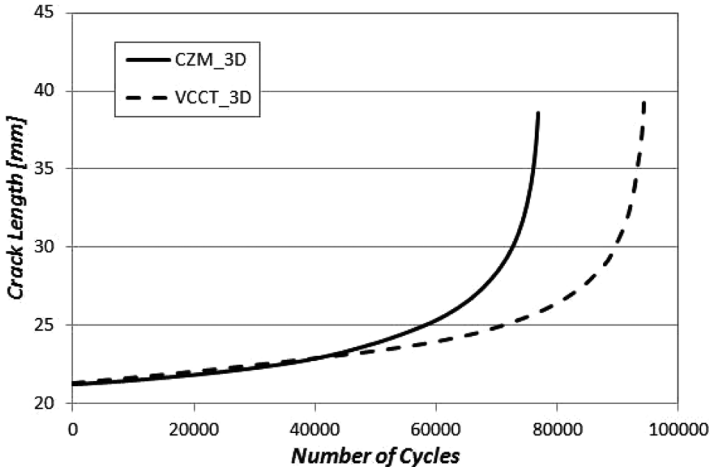

FIGURE 13 Comparison of *a*–*N* values in the case of ELS obtained by CZM and VCCT.

3.1.3. Mixed-mode I/II loading (MMELS)

Figure 14 shows the values of G_I and G_{II} obtained by CZM and VCCT, along with G and *MM*. The values obtained with the two methods in this case highlight a little bit the differences found for the single modes (see previous paragraph); however, the total G are instead almost superimposed (1% average difference from 21- to 30-mm crack length) and difference in mixed-mode ratio is not very large.

The main result in terms of crack length vs. number of cycles is shown in Fig. 15 where, skipping the first millimeter of propagation, the values are practically coincident (less than 1% difference).

3.2. Single-Lap Joint

Figure 16 shows the values of G_I and G_{II} obtained by CZM and VCCT, along with G and *MM*. Concerning the comparison of the single modes, the values are closer to each other than in the case of MMELS, except the first 3 mm, necessary to establish a steady state process zone in CZM. After this, the total G is the same and so also the mixed-mode ratio (2.5% average difference from 3- to 10-mm crack length).

With these premises, the crack length vs. number of cycles in Fig. 17, skipping the first millimeter of propagation, the values are practically coincident (4.5% difference at 10-mm crack length).

3.3. Calculation Time

The calculation times are reported in Table 3. The CZM results 2–15 times quicker than VCCT, despite a far less powerful computation hardware.

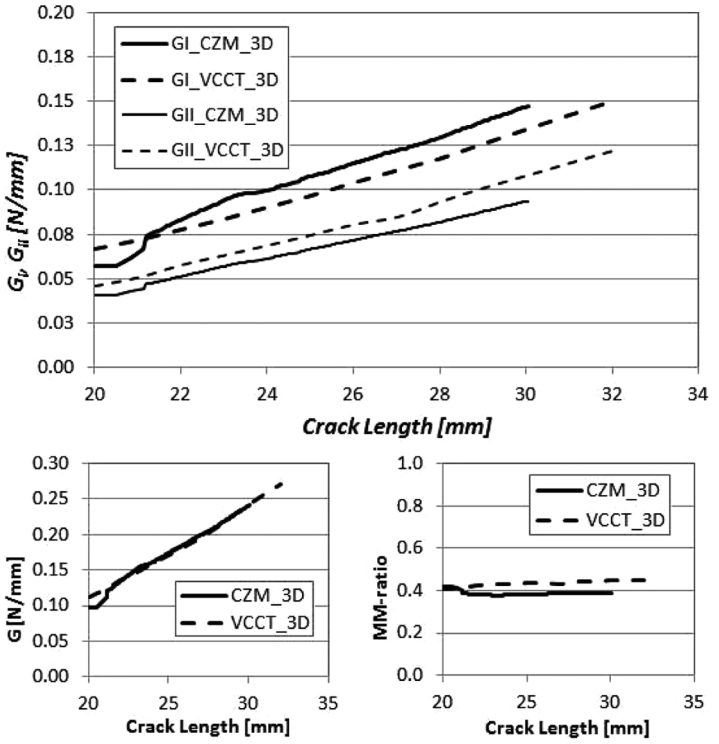

FIGURE 14 Comparison of G_I, G_{II}, G, and MM obtained by CZM and VCCT in the case of MMELS.

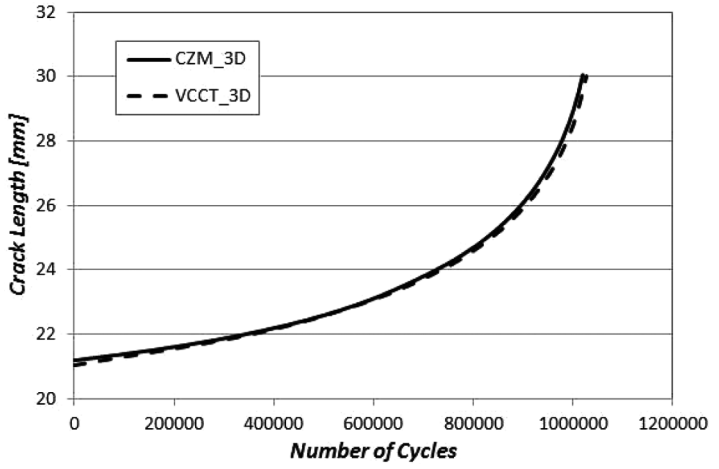

FIGURE 15 Comparison of a–N values in the case of MMELS obtained by CZM and VCCT.

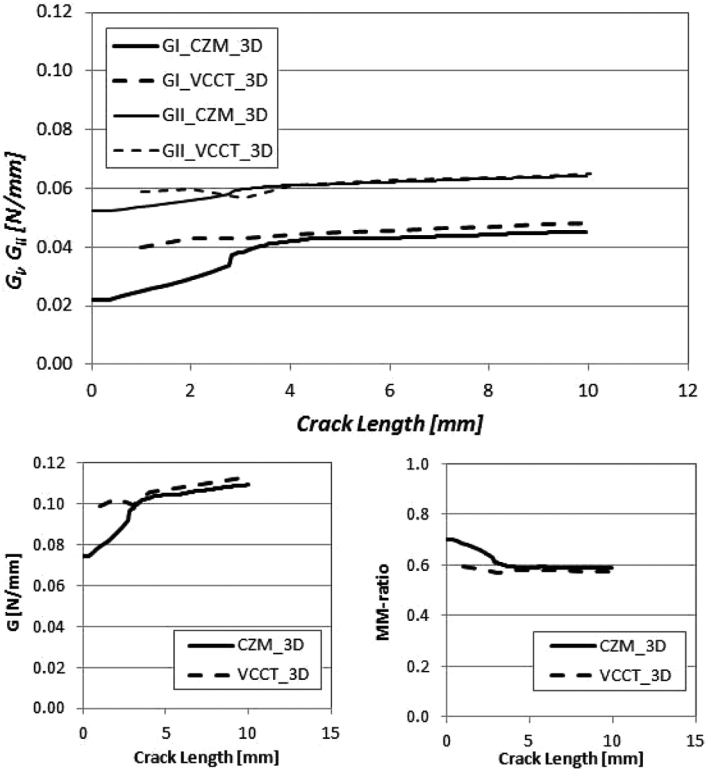

FIGURE 16 Comparison of G_I, G_{II}, G, and MM obtained by CZM and VCCT in the case of SLJ.

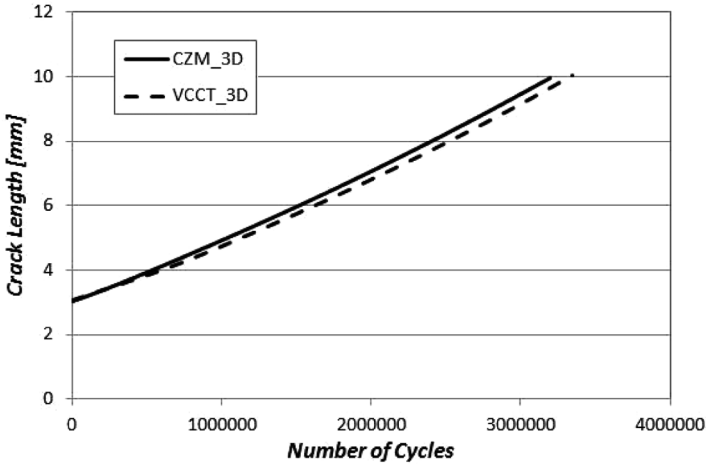

FIGURE 17 Comparison of a–N values in the case of SLJ obtained by CZM and VCCT.

TABLE 3 Calculation Time (Minutes per 10 mm Crack Growth)

	DCB	ELS	MMELS	SLJ
CZM	181	56	79	39
VCCT	343	314	1168	514

The origin of this large difference in performance between the in-house built CZM subroutine and the built-in VCCT, both run using the Abaqus solver, can be at least partly found in the direct cyclic procedure that is associated with VCCT in Abaqus. Indeed, this procedure requires quite a large number of iterations to satisfy convergence on ΔG value. On the other hand, relaxing the convergence on ΔG may affect the number of cycles to failure in a hardly predictable way.

4. CONCLUSIONS

The comparison of the performances of CZM [21] and VCCT embedded in the software Abaqus on mode I, mode II, and mixed-mode I/II loaded cracks in composite assemblies yielded the following results:

- The two models are in overall good agreement with each other, with the exception of the first instants of propagation where the CZM process zone has to shape up, whereas the VCCT starts with a sharp crack.
- While the modeling effort is a bit higher (need of introducing a layer of cohesive elements), the CZM is of easier use (no need to identify the proper number of Fourier terms and time increment to represent cyclic loading). At the same time, it results more efficient as the computation is lower up to one order of magnitude, despite the less performing hardware used to run the analyses.

FUNDING

The work of A. Bernasconi concerning VCCT was supported by Regione Lombardia in the framework of the project "STIMA—Strutture Ibride per Meccanica ed Aerospazio"—Bando Accordi Istituzionali—ID_Progetto: 14567. The work of F. Moroni was supported by Emilia-Romagna Region (POR FSE 2007–2013).

REFERENCES

[1] Paris, P., and Erdogan, F., *J. Basic Eng.* **85**, 528–534 (1961).
[2] Curley, A. J., Hadavinia, A., Kinloch, A. J., and Taylor, A. C., *Int. J. Fract.* **103**, 41–69 (2000).

[3] Forman, F. G., Kearnay, V. E., and Engle, R. M., *J. Basic Eng. Trans. ASME 89* **885**, 459 (1967).
[4] Pirondi, A., and Moroni, F., *Int. J. Adhes. Adhes.* **29**, 796–805 (2009).
[5] Hutchinson, J. W., and Evans, A. G., *Acta Mater.* **48**, 125–135 (2000).
[6] Blackman, B. R. K., Hadavinia, H., Kinloch, A. J., and Williams, J. G., *Int. J. Fract.* **119**, 25–46 (2003).
[7] Li, S., Thouless, M. D., Waas, A. M., Schroeder, J. A., and Zavattieri, P. D., *Compos. Sci. Technol.* **65**, 281–293 (2005).
[8] Maiti, S., and Geubelle, P. H., *Eng. Fract. Mech.* **72**, 691–708 (2005).
[9] Yang, Q. D., Thouless, M. D., and Ward, S. M., *J. Mech. Phys. Solids* **47**, 1337–1353 (1999).
[10] Roe, K. L., and Siegmund, T., *Eng. Fract. Mech.* **70**, 209–232 (2003).
[11] Muñoz, J. J., Galvanetto, U., and Robinson, P., *Int. J. Fatigue* **28**, 1136–1146 (2006).
[12] Turon, A., Costa, J., Camanho, P. P., and Dávila, C. G., *Compos. Part A* **38**, 2270–2282 (2007).
[13] Khoramishad, H., Crocombe, A. D., Katnam, K. B., and Ashcroft, I. A., *Int. J. Fatigue* **32**, 1146–1158 (2010).
[14] Khoramishad, H., Crocombe, A. D., Katnam, K. B., and Ashcroft, I. A., *Eng. Fract. Mech.* **78**, 3212–3225 (2010).
[15] Naghipour, P., Bartsch, M., and Voggenreiter, H., *Int. J. Solid Struct.* **48**, 1070–1081 (2011).
[16] Harper, P. W., and Hallett, S. R., *Int. J. Fatigue* **32**, 1774–1787 (2010).
[17] Beaurepaire, P., and Schuëller, G. I., *Eng. Fract. Mech.* **78**, 2399–2413 (2011).
[18] Allegri, G., and Wisnom, M. R., *Int. J. Fatigue* **43**, 226–234 (2012).
[19] Moroni, F., and Pirondi, A., *Eng. Fract. Mech.* **89**, 129–138 (2012).
[20] Moroni, F., and Pirondi, A., *ECCM15– 15th European Conference on Composite Materials, Venice, Italy, 24–28 June* (2012).
[21] Moroni, F., Pirondi, A., and Giuliese, G., *IGF XXII– 22nd Congress of the Italian Group on Fracture, Rome, Italy, 1–3 July* (2013).
[22] Rybicki, E. F., Kanninen, M. F., *Eng. Fract. Mech.* **9**, 931–938 (1977).
[23] Raju, I. S., *Eng. Fract. Mech.* **28**, 251–274 (1987).
[24] Shivakumar, K. N., Tan, P. W., and Newman Jr. J. C., *Int. J. Fract.* **36**, 43–50 (1988).
[25] Sun, C. T., and Jih, C. J., *Eng. Fract. Mech.* **28**, 13–20 (1987).
[26] Whitcomb, J. D., *J. Compos. Mater.* **26**, 1523–1535, ISSN 0021-9983 (1992).
[27] Hutchinson, J. W., and Suo, Z. *Advances in Applied Mechanics*, (Academic Press, New York, 1992), p. 28.
[28] Harbert, S. J., and Hogan, H. A., *Am. Soc. Mech. Eng. Pet. Div. Publ PD* **45**, 107–112 (1992).
[29] Salpekar, S. A., O'Brien, T. K., and Shivakumar, K. N., *J. Compos. Mater.* **30** (4), 418–440 (1996).
[30] Fawaz, S. A., *Eng. Fract. Mech.* **59**, 3, 327–342 (1998).
[31] Beuth, J. L., Narayan, S. H., *ASTM Spec. Tech. Publ.* **1285**, 324–342 (1997).
[32] Shen, F., Lee, K. H., and Tay, T. E., *Compos. Sci. Technol.* **61**, 1239–1251 (2001).
[33] O'Brien, T. K., Characterization, analysis and prediction of delamination in composites using fracture mechanics, *Oral Reference Number: ICF100942OR* (2001).

[34] Zou et al., *Int. J. Solid Struct.* **38**, 2597–2613 (2001).
[35] Cheuk, P. T. et al., *Compos. Struct.* **57**, 109–115 (2002).
[36] Krueger, R., *Appl. Mech. Rev.* **57**, 109–143 (2004).
[37] Okada, H., Higashi, M., Kikuchi, M., Fukui, Y., and Kumazawa, N., *Eng. Fract. Mech.* **72**, 1717–1737, ISSN 0013-7944 (2005).
[38] Murri, G. B., and Schaff, J. R., *Compos. Sci. Technol.* **66**, 499–508 (2006).
[39] Xie, D., Waas, A. M., Shahwan, K. W., Schroeder, J. A., and Boeman, R. G., *CMES—Comp. Model Eng. Sci.* **6**, 515–524 (2004).
[40] Xie, D., Chung, J., Waas, A. M., Shahwan, K. W., Schroeder, J. A., Boeman, R. G., Kunc, V., Klett, L. B., *Int. J. Fract.* **134**, 231–250 (2005).
[41] Xie, D., and Biggers Jr, S.B., *Finite Elem. Anal. Des.* **42**, 977–984 (2006).
[42] Marannano, G. V., Mistretta, L., Cirello, A., Pasta, S., *Eng. Fract. Mech.* **75**, 5122–5133 (2008).
[43] Leski, A., *Finite Elem Anal. Des.* **43**, 261–268 (2007).
[44] Krueger, R., NASA/CR-2010-216723, *NIA Report No. 2010-04* (2010).
[45] Pietropaoli, E., and Riccio, A., *Compos. Sci. Technol.* **70**, 1288–1300 (2010).
[46] Pietropaoli, E., and Riccio, A., *Compos. Sci. Technol.* **71**, 836–846 (2011).
[47] Liu, P. F., Hou, S. J., Chu, J. K., Hub, X. Y., Zhou, C. L., Liu, Y. L., Zheng, J. Y., Zhao, A., and Yana, L., *Compos. Struct.* **93**, 1549–1560 (2011).
[48] Ye, C., Shi, J., Cheng, G. J., *Int. J. Fatigue* **44**, 151–156 (2012).
[49] Lemaitre, J., *J. Eng. Mater. Technol.* **107**, 83–89 (1985).
[50] Harper, W. P., and Hallett, S. R., *Eng. Fract. Mech.* **75**, 4774–4792 (2008).
[51] Rice, J. R., *J. Appl. Mech.* **35**, 379–386 (1968).
[52] Pirondi, A., and Moroni, F., Simulating fatigue failure in bonded composite joints using a modified cohesive zone model. In: *Composite Joints and Connections*, Camanho, P. P., and Tong, L. (Eds.), (Woodhead Publishing Ltd., Cambridge, UK, 2011).
[53] Ungsuwarungsru, T., and Knauss, W. G., *Int. J. Fract.* **35**, 221–241 (1987).
[54] Kenane, M., and Benzeggagh, M. L., *Compos. Sci. Technol.* **56**, 439–449 (1996).
[55] Kenane, M., and Benzeggagh, M. L., *Compos. Sci. Technol.* **57**, 597–605 (1997).
[56] Moroni, F., and Pirondi, A., *J. Adhes.* **86**, 1–21 (2010).